JACS
JOURNAL OF THE AMERICAN CHEMICAL SOCIETY
pubs.acs.org/JACS
Article

Two-Stage Solvation of Lithium Polysulfides in Working Lithium−Sulfur Batteries

Xi-Yao Li, Bo-Quan Li,* Shuai Feng, Zheng Li, Liang Shen, Shu-Yu Sun, Zi-Xian Chen, Tian Jin, Xiang Chen, Meng Zhao, Xue-Qiang Zhang, Jia-Qi Huang, and Qiang Zhang*

Cite This: J. Am. Chem. Soc. 2025, 147, 15435−15447
Read Online
ACCESS | Metrics & More | Article Recommendations | Supporting Information

ABSTRACT: Lithium−sulfur (Li−S) batteries are promising in achieving high energy density but inferior in cycling lifespan since Li polysulfides (LiPSs) corrode Li metal anode. Weakening the electrolyte solvating power (ESP) for LiPSs effectively mitigates anodic corrosion but inevitably retards cathodic reaction kinetics. Herein, the correlation between the ESP and the LiPS redox kinetics in weakly solvating electrolyte is unveiled for achieving high-performance Li−S batteries. The ESP exhibits a two-stage variation tendency as the weakly solvating solvent (WSS) content increases, where the transition depends on whether the WSS enters the LiPS inner solvation shell. Once the WSS directly coordinates with LiPSs, the LiPS charge-transfer kinetics deteriorate dramatically, with a rapid increase in activation polarization. To overcome the kinetic sluggishness, advanced electrocatalysts are introduced to endow Li−S batteries with reduced polarization and prolonged cycling lifespan. An ultrahigh energy density of 607 W h kg^{-1} is realized in 10 Ah-level pouch cells with a stable cycling lifespan. This work deepens the current understanding of LiPS solvation and kinetics, highlighting the significance of weakly solvating electrolytes toward high-energy-density and long-cycling Li−S batteries.

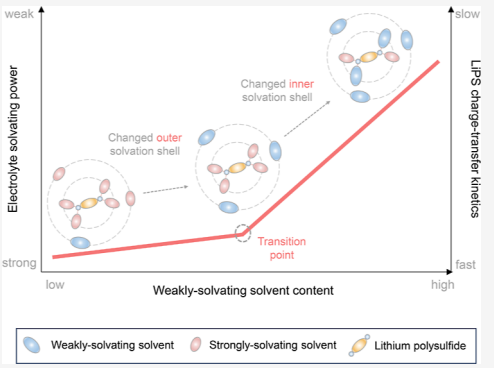

INTRODUCTION

Electrolyte constitutes the blood of working batteries.[1−3] The physical and chemical properties of electrolyte directly determine the anodic and cathodic behaviors and further battery performances.[4−7] For the batteries employing soluble electrode active materials to achieve high energy density[8−11] or long cycling stability,[12−14] the correlation between the electrolyte solvating power (ESP) for the soluble active species and the redox kinetics of the electrode active materials is crucial for probing the electrochemical mechanism as well as promoting the overall battery performances.

Lithium−sulfur (Li−S) batteries are promising next-generation rechargeable batteries with an ultrahigh theoretical energy density of up to 2600 W h kg^{-1}.[15−18] Soluble Li polysulfides (LiPSs) connect the solid charge and discharge products of S_8 and Li_2S in sulfur cathodes and serve as key intermediates.[19−23] Ether-based electrolytes currently constitute the benchmark for Li−S battery research and applications, typically composed of 1,3-dioxolane (DOL) and 1,2-dimethoxyethane (DME).[24−27] These mixed solvents dissolve massive LiPSs to guarantee smooth cathodic conversion kinetics and full delivery of high discharge capacity and energy density.[28−31] However, the parasitic reactions between the LiPSs and Li metal anodes result in unsatisfactory cycling stability of Li−S batteries in DOL/DME-based electrolytes.[32−35] Previous researches have demonstrated that employing weakly solvating electrolytes (WSEs) by incorporating weakly solvating solvents (WSSs) into the DOL/DME benchmark can effectively diminish the LiPS corrosion on Li metal anodes and enhance the cycling stability of Li−S batteries.[36−39] Nevertheless, the WSEs inevitably retard the LiPS cathodic conversion kinetics, leading to deteriorated cell polarization, reduced discharge capacity, and low energy density at the pouch cell level.[40−44] The current chemical understandings impute the above dilemma to the decreased LiPS solubility.[45−47] However, molecular-level insights into the ESP and the solvation structure of the dissolved LiPSs remain elusive, though their importance has been widely acknowledged in prominently determining the electrochemical behaviors of both the sulfur cathode and the Li anode.[48−50] A direct correlation between the ESP and the LiPS redox kinetics has not yet been established, resulting in the blindness of the WSE design in promoting Li−S battery performances.

In this contribution, the ESP and the LiPS redox kinetics in WSEs are correlated to guide the construction of practical high-energy-density and long-cycling Li−S batteries. Concretely, the activation polarization corresponding to LiPS

Received: January 25, 2025
Revised: April 11, 2025
Accepted: April 14, 2025
Published: April 22, 2025

https://doi.org/10.1021/jacs.5c01588
J. Am. Chem. Soc. 2025, 147, 15435−15447

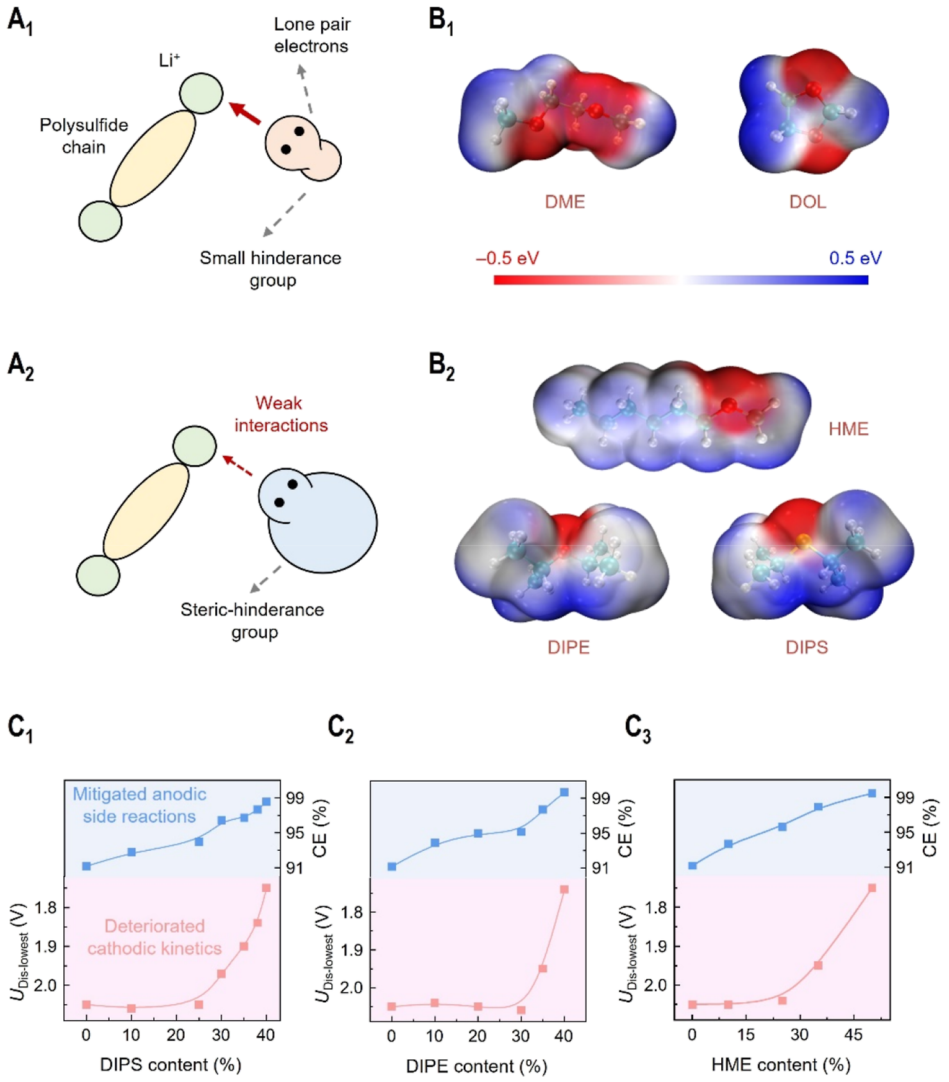

Figure 1. The rules to weaken the ESP and corresponding impacts on anode and cathode performances. (A) Illustration of the interactions between LiPSs and (A_1) SSS or (A_2) WSS. (B) Molecular structure and electrostatic potential (isovalue = 0.001 au) of the representative (B_1) SSSs (DME and DOL) and (B_2) WSSs (DIPS, DIPE, and HME). The hydrogen, carbon, oxygen, and sulfur atoms are marked with white, blue, red, and yellow, respectively. (C) The $U_{Dis\text{-}lowest}$ (marked in red) and Coulombic efficiency (marked in blue) of Li−S cells with increasing WSS contents with (C_1) DIPS, (C_2) DIPE, and (C_3) HME electrolytes, respectively (sulfur loading: 4.0 mg_S cm^{-2}).

interfacial charge-transfer kinetics exhibits a two-stage variation tendency with increased WSS contents, as indicated by the polarization decoupling results, wherein a transition point is identified by a two-stage activation polarization variation with different increasing rates before and thereafter. Further quantitative nuclear magnetic resonance (NMR) analysis reveals that the ESP also exhibits a two-stage variation tendency akin to the activation polarization, with the transition being contingent upon whether the WSS enters the LiPS inner solvation shell and directly coordinates with LiPSs. Both distribution of relaxation time (DRT) analysis and density functional theory (DFT) calculations elucidate that direct coordination of the WSS with LiPSs results in significant deterioration of the intrinsic LiPS redox kinetics due to the rapid increase in activation energy in the rate-determining step. To overcome the sluggish charge-transfer kinetics and reduce the activation polarization under high-WSS-content conditions, advanced electrocatalysts are introduced to regulate the energy and chemical states of LiPSs at the cathodic interface. Consequently, the electrocatalyst-enhanced WSEs enable 2 Ah-level Li−S pouch cells achieve 100 stable cycles and rechargeable 10 Ah-level Li−S pouch cells attain an ultrahigh energy density of 607 W h kg^{-1} with 17 cycles, calculated based on the total mass of all the cell components.

RESULTS AND DISCUSSION

Correlation between WSEs and Battery Polarization.

The solvation interaction between solvents and LiPSs is governed by coordination between the electronegative sites in the solvent molecules and the electropositive sites in the LiPS molecules (Figure 1A_1). Introducing huge steric-hindrance groups adjacent to these coordination sites in the solvent molecules constitutes an effective approach to weaken the solvents' solvating power (Figure 1A_2). Three typical WSSs featuring huge steric hindrance, including hexyl methyl ether (HME), di-isopropyl ether (DIPE), and di-isopropyl sulfide (DIPS), are employed as cosolvents in electrolyte to weaken the ESP (Figure S1). The calculated electrostatic potential evidently illustrates the above steric-hindrance effect, showing a more dispersed electronegative region in strongly solvating

https://doi.org/10.1021/jacs.5c01588
J. Am. Chem. Soc. 2025, 147, 15435−15447

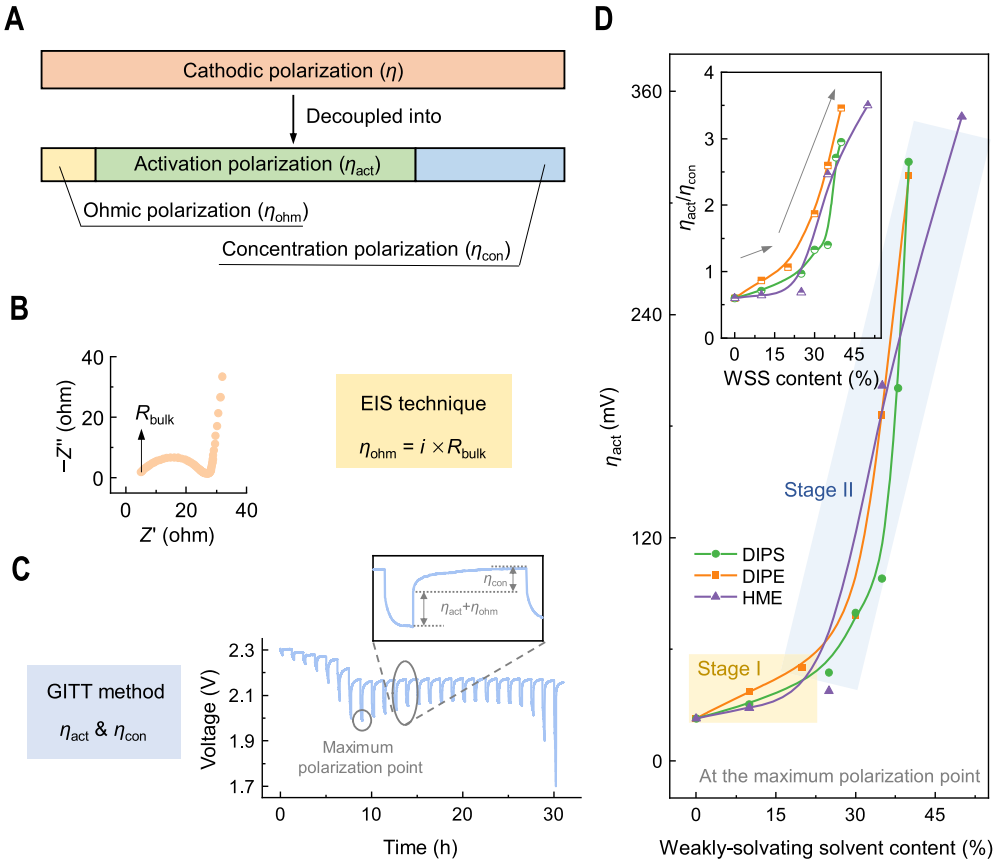

Figure 2. The cathodic polarization decoupling and variation tendency with increasing WSS contents. (A) Components of the cathodic polarizations. (B) Decoupling the η_{ohm} through the EIS technique. (C) Decoupling the η_{act} and η_{con} through GITT methods. (D) Polarization evolution when reducing the WSS content (inset: the η_{act} to η_{con} ratio versus the WSS content). Notably, all these measurements are based on Li−S full cells with a sulfur loading of 4.0 mg_S cm^{-2}.

solvents (SSSs) such as DOL and DME compared with WSSs (Figure 1B). Further, the natural bond orbital charges of the ligand atom (oxygen or sulfur) in WSS and SSS molecules are calculated to quantify the solvents' solvating power (Figure S2), revealing that charges in DOL (0.59*e*) and DME (0.57*e*) are significantly more negative than those in HME (0.29*e*), DIPE (0.25*e*), and DIPS (0.066*e*). The above examinations suggest that varying the ratios of WSS and SSS in electrolyte can effectively construct WSEs with different ESPs, where an increase in the WSS content leads to weakened ESP. In addition, either DIPE, DIPS, or HME and DOL/DME are soluble with each other at any proportion, which guarantees the feasibility to continuously reduce the ESP by tuning the DIPE, DIPS, or HME content in electrolyte.

Consistent with the electrochemical behaviors reported by previous literature,[37,45,46] all of the WSEs, whether constructed by DIPS, DIPE, or HME solvents, exhibit anodic protection and cathodic deterioration in Li−S batteries (Figure S3). To quantitatively analyze the effect of the different ESPs on the apparent anodic protection effect and the cathodic kinetics behaviors, Coulombic efficiency (CE) and the lowest voltage during the discharge process ($U_{Dis\text{-}lowest}$, the point between the first and the second discharge plateau defined by $dU/dQ = 0$, U and Q are the discharge voltage and capacity, respectively) are selected as the two indicators (Figure 1C). Note that the polarization contribution of the anode is small enough to be ignored at a small rate of 0.1 C based on previous reports.[51] As the WSS content increases from 0 to 40%, the CE rises from ca. 91% to 99%, suggesting mitigated anodic side reactions. On the contrary, the $U_{Dis\text{-}lowest}$ drops from ca. 2.05 V to below 1.80 V, illustrating unfavorable cathodic redox kinetics. Notably, the drop tendency of $U_{Dis\text{-}lowest}$ is not linearly correlated to the WSS content. Instead, there is a transition point where $U_{Dis\text{-}lowest}$ remains stable before it drops rapidly thereafter.

To fully comprehend the observed sudden deterioration of the cathodic redox kinetics, we evaluated the cathodic polarization during the discharge process. In principle, the cathodic polarization can be decoupled into Ohmic polarization (η_{ohm}), activation polarization (η_{act}), and concentration polarization (η_{con}). Concretely, η_{ohm} follows Ohm's Law, η_{act} is caused by the charge-transfer resistance dictated by the Bulter−Volmer equation, and η_{con} results from mass-transport limitations governed by the Nernst−Planck equation (Figure 2A). To accurately distinguish each part from the overall polarization, a galvanostatic intermittent titration technique combining electrochemical impedance spectroscopy (GITT−EIS) method was conducted in Li−S cells. In detail, the bulk resistance (R_{bulk}) is determined from the high-frequency intercept of the EIS Nyquist plot, and η_{ohm} can be obtained through multiplying R_{bulk} by the applied current i (Figure 2B). During GITT upon removal of the applied current in the relaxation step, the immediate voltage increment is attributed to the elimination of η_{ohm} and η_{act} due to their current-dependent properties (Figure 2C, inset). Afterward, the voltage gradually approaches the thermodynamic potential (vs Li/Li^+) over the relaxation period, and the corresponding

https://doi.org/10.1021/jacs.5c01588
J. Am. Chem. Soc. 2025, 147, 15435−15447

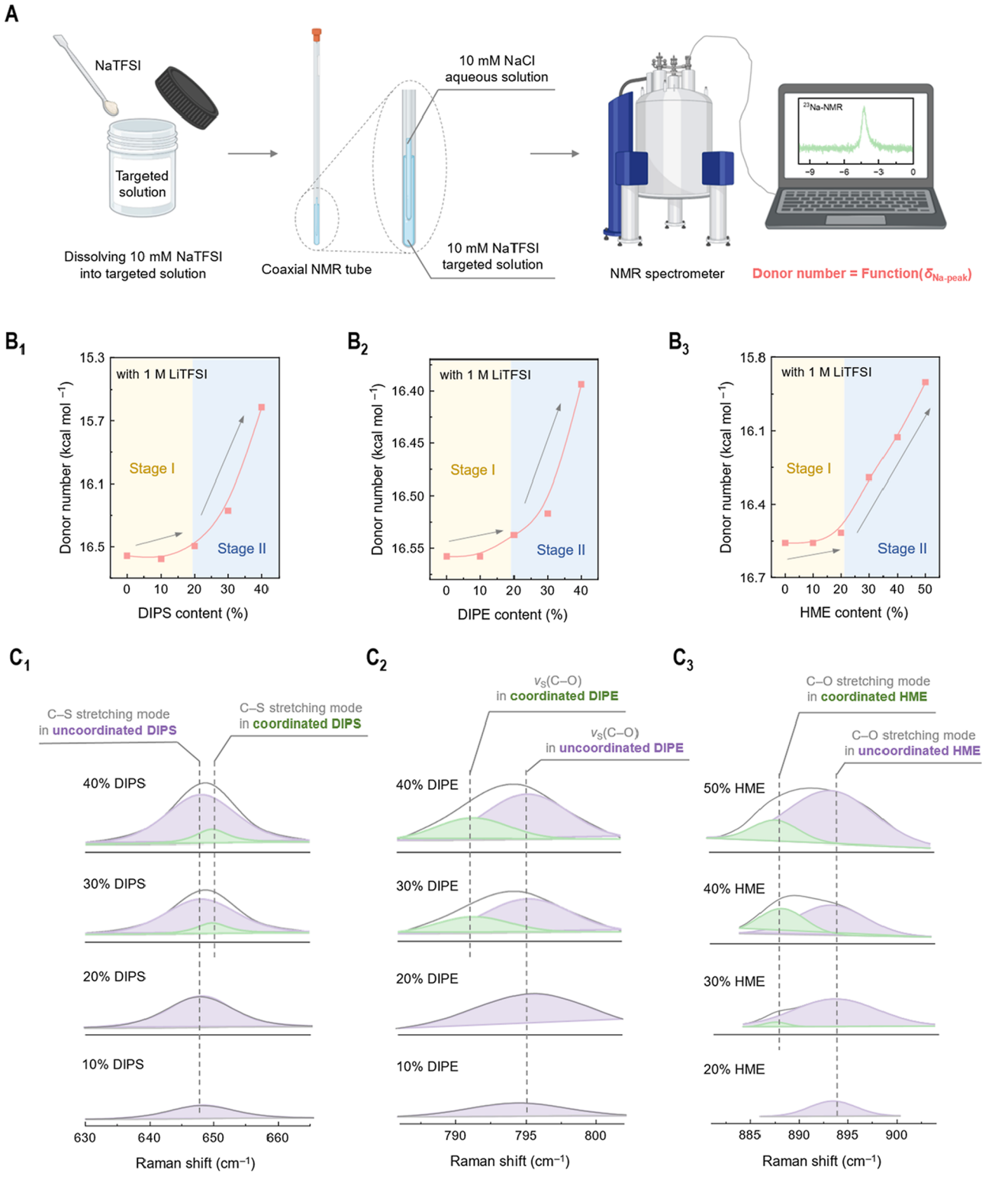

Figure 3. Quantifications of the ESP and the solvation structures in WSEs. (A) Illustrations of DN measurements to quantify the ESP by ^{23}Na NMR spectroscopy. (B) DN evolutions of WSEs with increasing (B_1) DIPS, (B_2) DIPE, and (B_3) HME contents. (C) Gaussian deconvolution of Raman signals into two separate vibration modes of coordinated and uncoordinated solvents with Li^+, enabling quantification of the solvation structures in electrolytes.

voltage rise is identified as the η_{con}. Therefore, the values of η_{ohm}, η_{act}, and η_{con} at various depths of discharge can be precisely determined through the GITT−EIS method (Figures S4−S10). Notably, the thermodynamic potential hardly changes during the discharge process, illustrating that the rapid drop of $U_{Dis\text{-}lowest}$ is caused by the sluggish kinetics rather than thermodynamic issues.

During the discharge process, the η_{ohm} consistently takes the smallest proportion across all the electrolyte systems (<10 mV), manifesting ionic and electronic conductivity variations

https://doi.org/10.1021/jacs.5c01588
J. Am. Chem. Soc. 2025, 147, 15435−15447

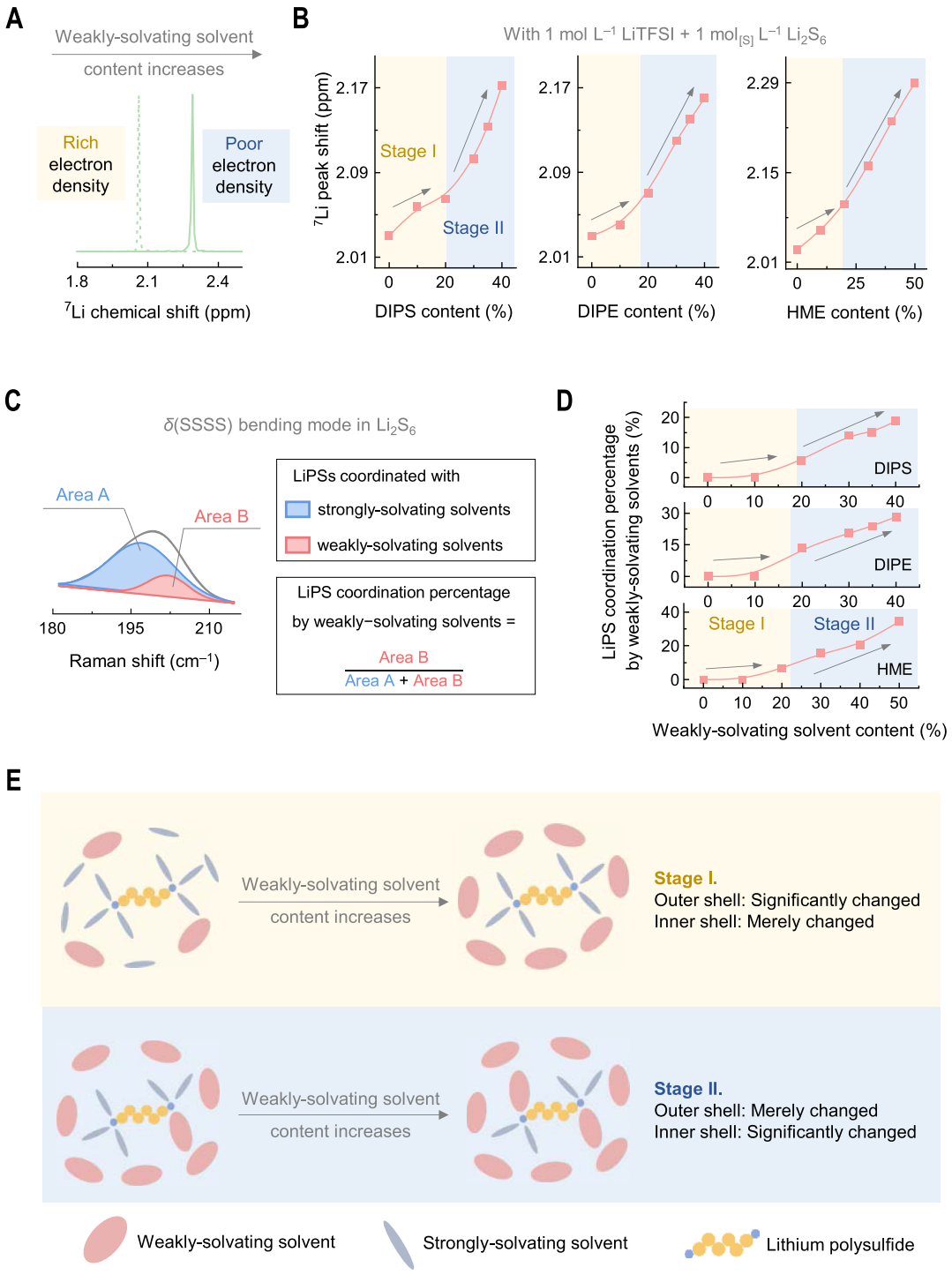

Figure 4. The correlation between the ESP and the solvation structure of LiPSs in WSEs. (A) Illustration of the Li nuclei electron density in LiPSs through ^{7}Li NMR peak shift. (B) ^{7}Li NMR peak shift evolutions versus the WSS content. (C) Illustration of the δ(SSSS) bending mode in LiPS molecules in Li_2S_6 solutions, with the signals Gaussian deconvoluted into two parts representing LiPS coordinated by SSS or WSS. (D) Evolutions of LiPS coordination percentage by WSSs versus increasing WSS contents. (E) Schematic illustration of the LiPS double-shell solvating structure evolutions with increasing WSS contents.

are not the primary contribution to the overall polarization deterioration (Figures S5, S7, and S9). In comparison, η_{act} and η_{con} increase initially until they reach a polarization peak around a discharge capacity of 300 mA h g^{-1}, and then they reduce during the rest of the discharge process until approaching the discharge termination (Figure S10). Increasing the WSS content particularly affects the polarization at its maximum point between the first and second plateaus, where the LiPS concentration is the highest (circled in Figure 2C). Accordingly, the polarization variations at the maximum polarization point are investigated in particular (Figure 2D). Concretely, the η_{act} exhibits a two-stage variation tendency along with increased WSS content to perform a transition point at approximately 20% WSS content. The η_{act} remains relatively stable below this threshold (stage I) and then escalates sharply thereafter (stage II). Taking the DIPE system

https://doi.org/10.1021/jacs.5c01588
J. Am. Chem. Soc. 2025, 147, 15435−15447

as an example, η_{act} increases by 1.2 times from 22.8 to 50.1 mV as the DIPE content rises from 0 to 20%. The η_{act} then surges by 13 times to 314 mV when the DIPE content increases from 0 to 40%. The η_{con} exhibits a similar but less pronounced two-stage variation tendency compared with the η_{act}, as evidenced by the increased η_{act}/η_{con} ratios, particularly at high WSS contents (Figure 2D, inset). The η_{act}/η_{con} ratios also display a two-stage variation tendency with an increment of 0.6 and 2.0 times before and after the transition point, demonstrating that the η_{act} is the predominant factor governing the Li−S battery polarization and the primary kinetic challenge afforded by the high WSS content in WSEs. This phenomenon further signifies that the charge-transfer limitation, rather than mass transport or electron−ion conduction, primarily restricts the LiPS conversion kinetics in WSE-based Li−S batteries. The distinct two-stage behavior of the η_{act} indicates the molecular interactions and charge-transfer circumstances are significantly altered beyond a certain WSS content in the WSE systems.

Quantitative Correlation between ESP and LiPS Solvation Structures. To fully comprehend the mechanism behind the impact of different WSS contents on the apparent polarization variations, the ESP of the different electrolytes and the solvation structures of LiPSs within them are quantitatively analyzed. Specifically, the ESP is assessed using the Gutmann donor number (DN), which is a widely recognized semi-empirical indicator that quantitatively distinguishes the solvating capability through the energy change when solvates are coordinated with the surrounding solvents. Based on the established empirical relationships,[52,53] the DN values correlate with the ^{23}Na peak chemical shift in NMR spectroscopy (Figure 3A). Concretely, a trace amount of NaTFSI (10 mmol L^{-1}), serving as a molecular probe, was dissolved in targeted solutions and injected into the outer shell of the coaxial NMR tube, while a 10 mmol L^{-1} NaCl aqueous solution was injected into the inner shell as the internal standard for NMR peak correlation. Adopting the above setup, the ^{23}Na-NMR peak chemical shifts (δ) of some acknowledged-DN solvents are calibrated and linearly correlated to their DNs, following the relationship of $DN = 2.052 \times \delta + 25.32$ (Figure S11). Afterward, the DN values of the WSEs with different WSS contents were measured (Figures S12−S14). As the WSS content increases, the DN values initially reduce slowly (stage I in Figure 3B_1−B_3) until the WSS content reaches ca. 20% and then decreases sharply thereafter (stage II). Taking the DIPS system as an example, the DN value decreases minimally from 16.6 to 16.5 kcal mol^{-1} (a 0.6% change) as the DIPS content increases from 0 to 20%, then rapidly lessens to 15.6 kcal mol^{-1} (a 6.0% change) at the 40% DIPS content. The changes in the DN values manifest that the ESP of the WSEs exhibits a two-stage variation tendency as the WSS content increases, with a notable transition point at around 20% WSS content, which is consistent with the variation tendency of the decoupled polarization observed above.

To further reveal the chemical nature behind the two-stage variation tendency of ESP, fine Raman spectroscopy was employed to investigate the molecular interactions between the solvents and solvates. Concretely, Raman signals of pure solvents and WSEs with variable WSS contents were detected (Figures S15−S21). Special attention is given to the vibrational mode alterations of the C−S or C−O bonds in the WSS molecules, as these interactions exist around the coordinating atoms (sulfur in DIPS and oxygen in DIPE and HME, respectively; Figure 3C_1−C_3). In the DIPE-based electrolyte system, the Raman shift at 795.3 cm^{-1}, corresponding to the symmetric wagging vibration (ν_S) of C−O bond in uncoordinated DIPE molecules,[54] remains unchanged until the DIPE content reaches 20%. Above this concentration, the ν_S(C−O) peak downshifts and a new signal located at 791.4 cm^{-1} emerges, assigned to the vibration mode of coordinated DIPE molecules. There are also similar behaviors in the DIPS- and HME-based electrolyte systems. The newly emerged Raman signal indicates that the WSS coordinates directly with Li ion beyond the transition point,[55] demonstrating that the two-stage variation in the ESP observed in Figure 3B results from the changes in the microscopic solvation structure. Specifically, prior to this transition point (stage I), the ESP exhibits minimal change as the solvates scarcely interact with the WSSs directly. After this transition point (stage II), the ESP decreases sharply due to direct WSS coordination, where Li bonds form between the WSSs and Li ions in electrolytes[56] (detailed discussion in Figures S22 and S23). In summary, the WSS coordination status before and after the transition point directly induces the two-stage variation tendency of the ESP.

Furthermore, we focus on the LiPS solvation behaviors in WSEs and correlate the two-stage variation tendency of the ESP with the LiPS redox kinetics at the molecular level. 1.0 $mol_{[S]}$ L^{-1} Li_2S_6 in WSEs with varying WSS contents were prepared for the examination. Notably, 1.0 mol L^{-1} Li bis(trifluoromethanesulfonyl)imide (LiTFSI) was also added in the above LiPS solutions to simulate the actual solvation circumstance and match the battery working conditions. Observing the LiPS solvation structures from the perspective of the Li atom, we analyzed the electron states surrounding the Li nuclei using ^{7}Li NMR spectroscopy (Figures S24−S26). Due to the shielding effect in the magnetic field, a higher chemical shift in nuclei (i.e., the downfield shift) corresponds to lower electron density surrounded, suggesting Li bond formation between the Li atoms in LiPSs and the negative-charge regions in WSS with weaker electron-donating capability[57] (Figure 4A). As the WSS content increases, the ^{7}Li peak shift (δ_{Li}) increases nonlinearly, exhibiting a two-stage variation tendency of a slow increase in stage I followed by a rapid increase in stage II (Figure 4B). Taking the DIPE system as an example, the δ_{Li} changes by 0.01 ppm when the DIPE content increases from 0 to 10%, while the δ_{Li} change quadruples to a 0.05 ppm enlargement when the DIPE content rises from 20% to 30%. The different growth rates between these two stages indicate that the electron density reduction surrounding the Li nuclei varies nonlinearly with the WSS content, featuring a distinct transition point attributed to the LiPS solvation structure changes.

The LiPS solvation structure is further quantified through fine Raman spectroscopy, detecting characteristic bond vibrations in LiPSs, solvents, and Li salts (Figures S27−S29). Attributed to the WSS coordination discussed in Figure 3C, the stretching mode of C−O (or C−S) bonds in solvents and the bending mode of S−N−S bonds in LiTFSI molecules alter when increasing the WSS contents (Figures S30−S32). To quantify the WSS coordination percentage in the LiPS solvation shell, the in-plane bending vibration mode δ(SSSS) in LiPSs is Gaussian deconvoluted[58] (Figures 4C and S33−S35). Taking the HME system as an example, the Raman shifts at 197.0 and 202.6 cm^{-1} represent characteristic signals for LiPSs coordinated by SSS or WSS,[59] with their deconvoluted peak areas denoted as area A and area B, respectively. The WSS coordination percentage is calculated as area B/(area A +

https://doi.org/10.1021/jacs.5c01588
J. Am. Chem. Soc. 2025, 147, 15435−15447

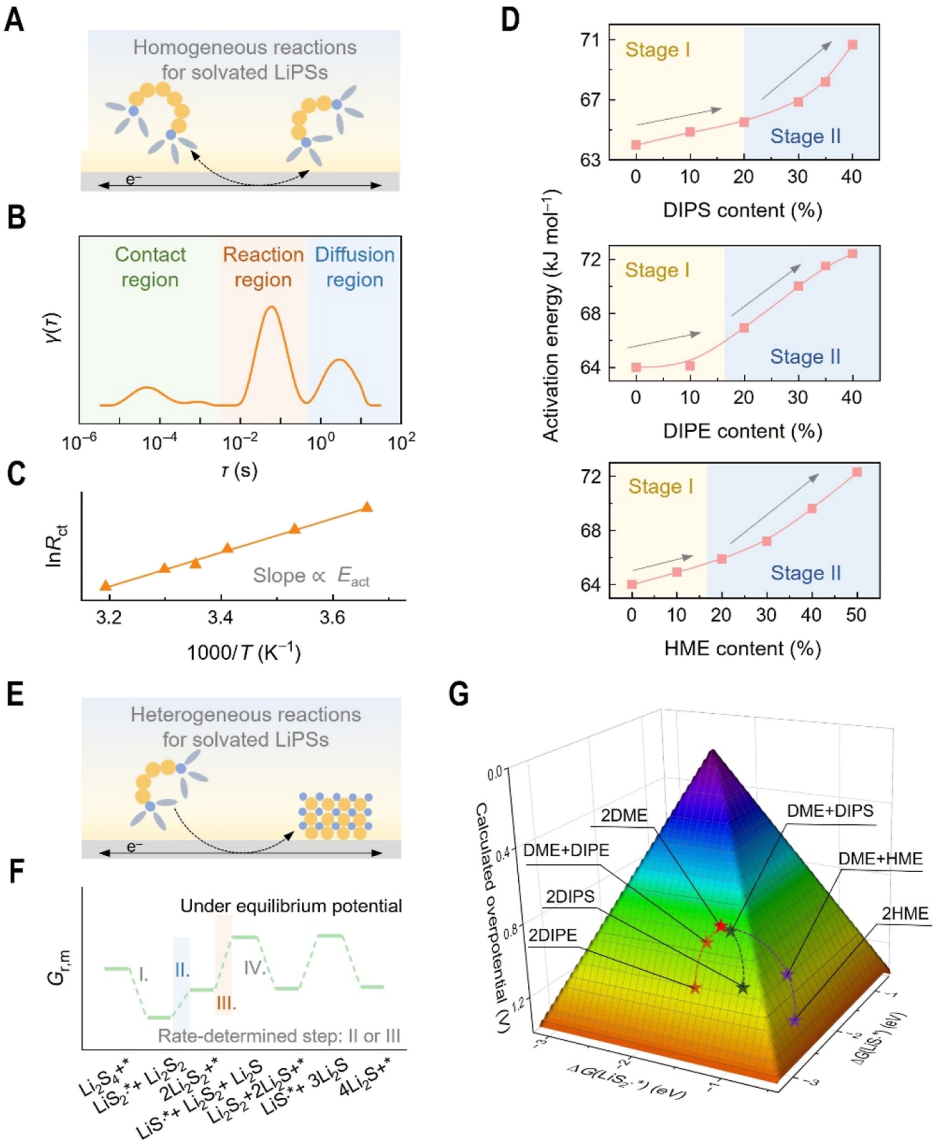

Figure 5. The correlation between the ESP and the LiPS redox kinetics in WSEs. (A) Illustration of homogeneous reactions for solvated LiPSs. (B) Schematic of DRT analysis in the Li_2S_6 symmetric cells. (C) Schematic of the E_{act} fitting for the LiPS homogeneous reactions through variable-temperature EIS tests. (D) E_{act} evolutions with increased WSS contents. (E) Illustration of heterogeneous reactions for solvated LiPSs. (F) Schematic of the Gibbs free energy evolution diagrams computed for solvated LiPSs under the equilibrium potential. (G) Three-dimensional volcano plots of calculated overpotential versus $\Delta G(LiS{\cdot}^*)$ and $\Delta G(LiS_2{\cdot}^*)$ corresponding to the LiPS heterogeneous reactions. The colors of red and blue represent the high and low overpotentials, respectively. The calculation results of LiPSs solvated by HME were obtained from our previous study.[44]

area B). Notably, the Raman shift of area B is ascertained through the LiPS vibration measurements in pure WSS. As the WSS content increases, the coordination percentage also exhibits a two-stage variation tendency (Figure 4D). In the DIPS system, the WSS coordination percentage remains zero below the 10% WSS content and rises to 5.67% at the 20% WSS content, manifesting few WSSs coordinate with LiPSs in stage I. After the transition point, the WSS coordination percentage jumps to 18.7% at the 40% WSS content, signifying that a non-negligible amount of LiPSs is coordinated by WSSs. Similar tendencies are also observed in the DIPE and HME systems. In summary, along with the WSS content increment, the LiPS solvation structures in WSEs change nonlinearly, displaying a two-stage variation tendency with a distinct transition point (Figure 4E). The transition dividing stage I and stage II depends on whether the WSS enters the LiPS inner solvation shell. In stage I, where the WSS content is relatively low, the WSSs primarily stay at the outer solvation shell of LiPSs since the WSSs are weaker in competing coordination with LiPSs than the SSSs. In stage II, with insufficient SSSs for full coordination of LiPSs and increased molecular entropy, the WSSs begin to enter the inner solvation shell and directly coordinate with LiPSs following the Li bond principle.[60] These changes in the LiPS solvation structure induced by WSS coordination result in a two-stage variation in the ESP and further affect the LiPS kinetic behaviors in Li−S batteries.

Evaluations of LiPS Redox Kinetics in WSEs. The above two-stage variation in LiPS solvation structure, driven by WSS coordination, closely mirrors the variation tendency of η_{act} exhibited in Figure 2D, suggesting a fundamental connection between the solvation structure and the redox kinetics of

https://doi.org/10.1021/jacs.5c01588
J. Am. Chem. Soc. 2025, 147, 15435−15447

LiPSs. Given that η_{act}, dominating the main polarization in batteries, is generated by the sluggish LiPS charge-transfer kinetics rather than mass transport or ion-electron conduction, we aim to associate WSS coordination with LiPS charge-transfer kinetics in both homogeneous and heterogeneous reactions.

To evaluate the homogeneous reactions between dissolved LiPSs, Li_2S_6 symmetric cells with WSEs were assembled, with EIS techniques employed for analysis (Figure 5A). To decouple the specific processes in the Nyquist plot, DRT analysis is adopted (Figure 5B), which identifies three peaks at the characteristic time (τ) of ca. 10^{-4}, 10^{-1}, and 10^{1} s, representing the contact, reaction, and diffusion region in the equivalent circuit, respectively[61] (Figure S36). Therein, the resistance in the reaction region (R_{ct}) quantitatively indicates the kinetic difficulty of LiPS charge transfer in the variable WSEs. As expected, the R_{ct} increases with reduced ESP (e.g., from 93.4 to 248 Ω as the DIPS content increases from 0 to 40% at room temperature, Figure S37). The activation energy (E_{act}), a fundamental kinetic indicator of the charge-transfer process, is then examined via EIS measurements and DRT analysis across different temperatures (T) from 0 to 40 °C (Figures S37−S45). E_{act} is fitted by plotting $\ln(R_{ct})$ against $1/T$ according to the Arrhenius equation (Figures 5C and S46). As the WSS content increases, the E_{act} displays a two-stage variation behavior (Figure 5D), e.g., in the DIPS system, the E_{act} increases by 1.5 kJ mol^{-1} when the DIPS content increases from 0% to 20% (stage I), and rises sharply by 5.2 kJ mol^{-1} from 20% to 40% (stage II). Notably, this transition point correlates with the states of whether the WSS directly coordinates with LiPSs, showing that the E_{act} of the reactions of the WSSs directly coordinated LiPSs is distinctly larger than that of the circumstance of the WSSs located at the LiPS outer solvation shell. The above results manifest that the charge-transfer kinetics of the LiPS homogeneous reactions become intrinsically more sluggish with reduced ESP once the WSSs penetrate the LiPS inner solvation shell.

To evaluate the LiPS heterogeneous reaction kinetics, DFT calculations for the conversion from Li_2S_4 to Li_2S were carried out (Figure 5E). Concretely, the solvation effect is presented by adding two solvent molecules (2 sol, i.e., 2DME, 2DIPS/DIPE/HME, or DME + DIPS/DIPE/HME) onto LiPS molecules and radicals (Figures S47−S49). According to our previous research,[62] the pathway of the sulfur reduction reaction is assumed to be the Li_2S_4 symmetrical decomposition, where Li_2S_4 initially converts to Li_2S_2 and then to Li_2S. The six-electron-transfer process can be decoupled into six steps as follows

$$(sol)_2{-}Li_2S_4 + (Li^+ + e^-) + * \rightarrow (sol)_2 - LiS_2{\cdot}* + Li_2S_2 \quad (I)$$

$$Li_2S_2 + (sol)_2{-}LiS_2{\cdot}* + (Li^+ + e^-) \rightarrow 2Li_2S_2 + * + 2sol \quad (II)$$

$$2Li_2S_2 + (Li^+ + e^-) + * + 2sol \rightarrow (sol)_2 - LiS{\cdot}* + Li_2S + Li_2S_2 \quad (III)$$

$$Li_2S + Li_2S_2 + (sol)_2 - LiS{\cdot}* + (Li^+ + e^-) \rightarrow 2Li_2S + Li_2S_2 + * + 2sol \quad (IV)$$

$$2Li_2S + Li_2S_2 + (Li^+ + e^-) + * + 2sol \rightarrow (sol)_2 - LiS{\cdot}* + 3Li_2S \quad (V)$$

$$3Li_2S + (sol)_2 - LiS{\cdot}* + (Li^+ + e^-) \rightarrow 4Li_2S + * + 2sol \quad (VI)$$

Therein, * represents graphene as the reaction substrate and Li_2S_2 and Li_2S are treated as crystals. Based on the above six steps, the Gibbs free energy evolution diagram is calculated and depicted at the equilibrium potential (E_{eq}) (Figures 5F and S50). Notably, reactions involving the WSS-coordinated LiPSs exhibit energy barriers higher than those coordinated by SSS (Tables S2−S4). Taking the HME system as an example, the energy barriers are 0.78 eV with 2DME, 0.87 eV with DME + HME, and 1.00 eV with 2HME, respectively. The enlarged energy barriers can be attributed to the higher binding energies of the LiPS radicals, which hinder the desorption process from the substrate and impede the subsequent reactions (Figure S51). The above energy variation results manifest that once the LiPS molecules and radicals are coordinated by WSS, the sudden drop in the ESP leads to inferior LiPS charge-transfer kinetics.

To identify the specific rate-determining step and overpotential in the LiPS heterogeneous reactions, two descriptors, $\Delta G(LiS_2{\cdot}*)$ and $\Delta G(LiS{\cdot}*)$, are introduced and defined as the Gibbs free energy changes of steps I and III (detailed discussion in Section 1.6.4. of Supporting Information). Based on the above two descriptors, steps I−IV can be quantitatively reflected by regions I−IV in the three-dimensional volcano plots (Figures 5G and S52). Concretely, all the systems locate in either region II or III, illustrating either step II or III can be the rate-determining step. These findings manifest that both the decomposition of $(sol)_2$-$LiS_2{\cdot}*$ and the generation of $(sol)_2$-$LiS{\cdot}*$ are kinetically unfavorable in the LiPS heterogeneous reactions. Furthermore, the WSS coordination increases the charge-transfer energy barrier in these rate-determining steps, hindering the overall LiPS redox kinetics and enlarging the overpotential of the LiPS heterogeneous reactions in WSEs (e.g., 0.78, 0.82, and 1.05 V for the systems of 2DME, DME + DIPE, and 2DIPE, respectively). Overall, based on the experimental and theoretical evaluations of both homogeneous and heterogeneous reactions, it is evident that direct coordination of WSS with LiPSs significantly lessens the ESP of the WSEs, which further reduces the intrinsic LiPS reactivity, hinders the cathodic charge-transfer kinetics, and sharply enlarges the cathodic activation polarization.

Electrocatalyst-Enhanced LiPS Redox Kinetics in WSEs. The WSEs with higher WSS contents and lower ESP potentially enhance the cycling life of Li−S batteries by inhibiting the anodic parasitic reactions, while the unbearable enlarged cathodic η_{act} induces rapid cathode failure. To leverage the advantages of WSEs while mitigating their drawbacks, aggravated η_{act} from WSS coordination must be optimized to an acceptable level. Modifying the cathodic interface with electrocatalysts presents an effective approach to regulate the LiPS cathodic charge-transfer kinetics independent of the LiPS solvation structure. In this way, introducing electrocatalysts into the cathodic compartment is expected to reduce η_{act} in WSEs. Titanium nitride (TiN) nanoparticles are adopted as model electrocatalysts due to their exceptional electrocatalytic performances[63−65] (Figures S53−S55).

https://doi.org/10.1021/jacs.5c01588
J. Am. Chem. Soc. 2025, 147, 15435−15447

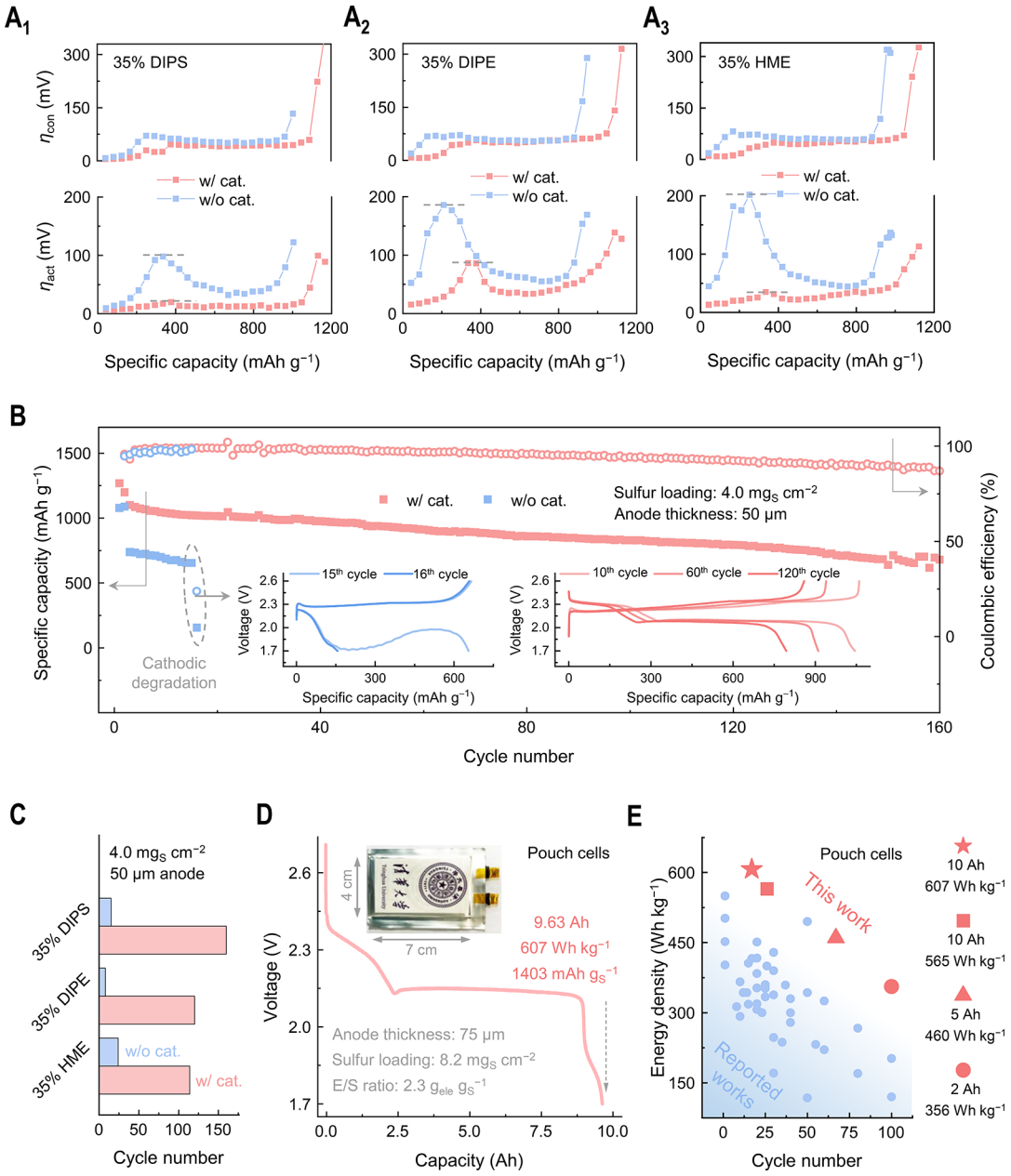

Figure 6. Electrocatalyst-enhanced Li−S full cells with WSEs. (A) The η_{act} and η_{con} evolutions in Li−S batteries with (A_1) DIPS, (A_2) DIPE, and (A_3) HME-based electrolyte with or without electrocatalysts. (B) Long-cycling performances and corresponding charge−discharge profiles (inset figures) for DIPS-based Li−S coin cells with or without electrocatalysts. (C) Comparisons on cycling life for DIPS, DIPE, or HME-based coin cells with or without electrocatalysts. (D) Optical photograph (inset) and the 1st cycle discharge profile of 10 Ah-level DIPS-based pouch cells with electrocatalysts. (E) Performance comparison of the rechargeable Li−S pouch cells between this work and other previously reported works. The energy densities are of the first cycle and calculated based on all the components including package and tabs.

The polarization distributions of the WSE-based Li−S batteries with or without electrocatalysts were analyzed by the GITT−EIS method (Figures S56 and 6A). As expected, introducing electrocatalysts significantly reduces the η_{act} while merely changes the η_{con} during the discharge process, indicating the electrocatalysts exclusively accelerate the charge-transfer kinetics in WSEs. For instance, in the 35% DIPS system, the maximum η_{act} is reduced from 98.1 to 20.0 mV, while the η_{con} remains unchanged at around 50 mV. The above results underscore the effectiveness of electrocatalysis in enhancing the charge-transfer kinetics and reducing the η_{act} in WSEs.

To concurrently achieve high cathodic and anodic performances, electrocatalysts and WSEs are employed in Li−S cells with thin anodes (50 μm) and high-loading cathodes (4.0 mg_S cm^{-2}). For the 35% DIPS system, the Li−S cells with electrocatalysts exhibit an ultrahigh specific capacity of 1269 mAh g^{-1} and maintain stable for over 160 cycles (Figure 6B). In comparison, the cells without electrocatalysts fail after only 15 cycles due to cathodic failure. During cycling, the charge−discharge voltage in the cells with electrocatalysts remains stable, whereas in the cells without electrocatalysts, the discharge voltage quickly drops to the cutoff point at the 16th cycle, leading to abrupt capacity loss (Figure 6B, inset). Similar behaviors are observed in the DIPE and HME systems

https://doi.org/10.1021/jacs.5c01588
J. Am. Chem. Soc. 2025, 147, 15435−15447

(Figures S57–S58), where the cells with electrocatalysts are endowed with prolonged cycling lifespan due to the mitigation of rapid cathodic failure in WSEs, while the cells without electrocatalysts suffer from a rapid polarization increase and capacity loss. Specifically, the cycling life extends from 8 to 120 cycles in the 35% DIPE system and from 24 to 114 cycles in the 35% HME system (Figure 6C). In brief, introducing electrocatalysts not only enhances the LiPS charge-transfer kinetics and reduces the cathodic polarization but also maintains the anodic stability in WSE-based Li–S batteries.

To evaluate the feasibility of combining WSEs and electrocatalysts in practical Li–S batteries, Ah-level pouch cells were assembled with a DIPS electrolyte and TiN electrocatalysts, which are uniformly embedded in cathodes (Figure S59). The 2 Ah-level pouch cells feature cathodes with a single-side sulfur loading of 7.4 mg_S cm^{-2}, anodes with a single-side thickness of 75 μm, and an electrolyte/sulfur (E/S) ratio of 3.8 g_{ele} g_S^{-1} (Figure S60 and Table S5). The pouch cell delivers an actual energy density of 356 W h kg^{-1} (based on all components including tabs and packages) and remains stable for 100 cycles. To further achieve higher energy density, 5 Ah-level pouch cells were assembled with a reduced E/S ratio of 2.8 g_{ele} g_S^{-1}, cathodes with a single-side sulfur loading of 7.6 mg_S cm^{-2}, and anodes with a single-side thickness of 75 μm. Consequently, the 5 Ah-level pouch cells deliver a superior actual energy density of up to 460 W h kg^{-1} and operate stably for 67 cycles (Figure S61).

To enhance the energy densities of pouch cells, the E/S ratio was further reduced, and the Cu current collectors were replaced into the ones with light mass (Table S6). In detail, 10 Ah-level pouch cells were assembled with the E/S ratio of 2.6 g_{ele} g_S^{-1}, cathodes with single-side sulfur loading of 8.2 mg_S cm^{-2}, and anodes with a single-side thickness of 75 μm to achieve 565 W h kg^{-1} with 26 stable cycles (Figure S62). Furthermore, the E/S ratio was reduced to 2.3 g_{ele} g_S^{-1} in another 10 Ah-level pouch cell with the same cell assembly parameters. Despite the extremely harsh conditions, the pouch cell delivers an ultrahigh specific capacity of 1403 mA h g^{-1} and a superior actual energy density of up to 607 W h kg^{-1} with 17 stable cycles (Figures 6D and S63). Notably, the energy densities of the above pouch cells are calculated based on all components, including tabs and packages. The above Ah-level pouch cells demonstrate leading performances in the Li–S field, excelling in both energy density and cycling lifespan (Figure 6E and Table S7). The simultaneously prolonged cycling lifespan and promoted energy density manifest the promise of employing WSEs in practical Li–S batteries once the cathodic kinetics are fully guaranteed (Figure S64).

CONCLUSIONS

The correlation between the ESP and the LiPS redox kinetics in WSEs is unveiled to guide the design of practical high-energy-density and long-cycling Li–S batteries. The ESP of WSEs exhibits a two-stage variation tendency as the WSS content increases, with a critical transition point depending on whether the WSS enters the LiPS inner solvation shell. Once the WSS directly coordinates with LiPSs, the LiPS intrinsic redox kinetics deteriorate dramatically with a sharp increase in activation energy and activation polarization. To overcome this kinetic sluggishness, advanced electrocatalysts are introduced to endow Li–S batteries with reduced polarization and longer cycling lifespan under harsh working conditions. Electrocatalyst-enhanced WSEs enable 2 Ah-level pouch cells with 100 stable cycles and 10 Ah-level pouch cells to reach an ultrahigh actual energy density of 607 W h kg^{-1}. This work deepens the fundamental understanding of the solvation and kinetics of LiPSs in WSEs and inspires solvation–interface synergistic regulation toward high-energy-density and long-cycling Li–S batteries.

ASSOCIATED CONTENT

Supporting Information

The Supporting Information is available free of charge at https://pubs.acs.org/doi/10.1021/jacs.5c01588.

Complete experimental details, additional material characterization, and electrochemical performance (PDF)

AUTHOR INFORMATION

Corresponding Authors

Bo-Quan Li − *Advanced Research Institute of Multidisciplinary Science, Beijing Institute of Technology, Beijing 100081, China; School of Materials Science and Engineering, Beijing Institute of Technology, Beijing 100081, China;* orcid.org/0000-0002-9544-5795; Email: libq@bit.edu.cn

Qiang Zhang − *Beijing Key Laboratory of Complex Solid State Batteries & Tsinghua Center for Green Chemical Engineering Electrification, Department of Chemical Engineering, Tsinghua University, Beijing 100084, China; Institute for Carbon Neutrality, Tsinghua University, Beijing 100084, China;* orcid.org/0000-0002-3929-1541; Email: zhang-qiang@mails.tsinghua.edu.cn

Authors

Xi-Yao Li − *Beijing Key Laboratory of Complex Solid State Batteries & Tsinghua Center for Green Chemical Engineering Electrification, Department of Chemical Engineering, Tsinghua University, Beijing 100084, China;* orcid.org/0000-0003-2366-8591

Shuai Feng − *College of Chemistry and Chemical Engineering, Taishan University, Shandong 271021, China;* orcid.org/0000-0002-8604-2097

Zheng Li − *Beijing Key Laboratory of Complex Solid State Batteries & Tsinghua Center for Green Chemical Engineering Electrification, Department of Chemical Engineering, Tsinghua University, Beijing 100084, China*

Liang Shen − *Beijing Key Laboratory of Complex Solid State Batteries & Tsinghua Center for Green Chemical Engineering Electrification, Department of Chemical Engineering, Tsinghua University, Beijing 100084, China*

Shu-Yu Sun − *Beijing Key Laboratory of Complex Solid State Batteries & Tsinghua Center for Green Chemical Engineering Electrification, Department of Chemical Engineering, Tsinghua University, Beijing 100084, China;* orcid.org/0000-0002-9942-8618

Zi-Xian Chen − *Advanced Research Institute of Multidisciplinary Science, Beijing Institute of Technology, Beijing 100081, China; School of Materials Science and Engineering, Beijing Institute of Technology, Beijing 100081, China;* orcid.org/0000-0002-9121-6506

Tian Jin − *Advanced Research Institute of Multidisciplinary Science, Beijing Institute of Technology, Beijing 100081, China; School of Materials Science and Engineering, Beijing Institute of Technology, Beijing 100081, China*

Xiang Chen − *Beijing Key Laboratory of Complex Solid State Batteries & Tsinghua Center for Green Chemical Engineering Electrification, Department of Chemical Engineering, Tsinghua University, Beijing 100084, China;* orcid.org/0000-0002-7686-6308

Meng Zhao − *Beijing Key Laboratory of Complex Solid State Batteries & Tsinghua Center for Green Chemical Engineering Electrification, Department of Chemical Engineering, Tsinghua University, Beijing 100084, China*

Xue-Qiang Zhang − *Advanced Research Institute of Multidisciplinary Science, Beijing Institute of Technology, Beijing 100081, China; School of Materials Science and Engineering, Beijing Institute of Technology, Beijing 100081, China;* orcid.org/0000-0003-2856-1881

Jia-Qi Huang − *Advanced Research Institute of Multidisciplinary Science, Beijing Institute of Technology, Beijing 100081, China; School of Materials Science and Engineering, Beijing Institute of Technology, Beijing 100081, China;* orcid.org/0000-0001-7394-9186

Complete contact information is available at: https://pubs.acs.org/10.1021/jacs.5c01588

Author Contributions

All authors have given approval to the final version of the manuscript.

Notes

The authors declare no competing financial interest.

■ ACKNOWLEDGMENTS

This work was supported by the National Key Research and Development Program (2021YFB2400300), the National Natural Science Foundation of China (22109007, T2322015, 22393900, 52394170, 22109086, 22209010), the China Postdoctoral Science Foundation (GZB20240346), the Shuimu Tsinghua Scholar Program of Tsinghua University, Xplorer Prize, and the Tsinghua University Initiative Scientific Research Program. The authors acknowledged the support from the Tsinghua National Laboratory for Information Science and Technology for theoretical simulations. We thank Yun-Wei Song, Qian Cheng, Jia−Jia Zhao, and Dr. Chang-Xin Zhao for helpful discussion.

■ REFERENCES

(1) Lu, D.; Li, R.; Rahman, M. M.; Yu, P.; Lv, L.; Yang, S.; Huang, Y.; Sun, C.; Zhang, S.; Zhang, H.; et al. Ligand-channel-enabled ultrafast Li-ion conduction. *Nature* **2024**, *627* (8002), 101−107.

(2) Hou, S.; Ji, X.; Gaskell, K.; Wang, P.-f.; Wang, L.; Xu, J.; Sun, R.; Borodin, O.; Wang, C. Solvation sheath reorganization enables divalent metal batteries with fast interfacial charge transfer kinetics. *Science* **2021**, *374* (6564), 172−178.

(3) Yao, Y.-X.; Xu, L.; Yan, C.; Zhang, Q. Principles and trends in extreme fast charging lithium-ion batteries. *EES Batteries.* **2025**, *1* (1), 9−22.

(4) Xu, J.; Zhang, J.; Pollard, T. P.; Li, Q.; Tan, S.; Hou, S.; Wan, H.; Chen, F.; He, H.; Hu, E.; et al. Electrolyte design for Li-ion batteries under extreme operating conditions. *Nature* **2023**, *614* (7949), 694−700.

(5) Yao, N.; Chen, X.; Fu, Z.-H.; Zhang, Q. Applying classical, ab initio, and machine-learning molecular dynamics simulations to the liquid electrolyte for rechargeable batteries. *Chem. Rev.* **2022**, *122* (12), 10970−11021.

(6) Zhang, Z.; Li, Y.; Xu, R.; Zhou, W.; Li, Y.; Oyakhire, S. T.; Wu, Y.; Xu, J.; Wang, H.; Yu, Z.; et al. Capturing the swelling of solid-electrolyte interphase in lithium metal batteries. *Science* **2022**, *375* (6576), 66−70.

(7) Liu, S.; Gu, B.; Chen, Z.; Zhan, R.; Wang, X.; Feng, R.; Sun, Y. Suppressing dendritic metallic Li formation on graphite anode under battery fast charging. *J. Energy Chem.* **2024**, *91*, 484−500.

(8) Li, M.; Wang, C.; Chen, Z.; Xu, K.; Lu, J. New concepts in electrolytes. *Chem. Rev.* **2020**, *120* (14), 6783−6819.

(9) Meng, Y. S.; Srinivasan, V.; Xu, K. Designing better electrolytes. *Science* **2022**, *378* (6624), No. eabq3750.

(10) Kondori, A.; Esmaeilirad, M.; Harzandi, A. M.; Amine, R.; Saray, M. T.; Yu, L.; Liu, T.; Wen, J.; Shan, N.; Wang, H.-H.; et al. A room temperature rechargeable Li_2O-based lithium−air battery enabled by a solid electrolyte. *Science* **2023**, *379* (6631), 499−505.

(11) Xie, C.; Wang, C.; Xu, Y.; Li, T.; Fu, Q.; Li, X. Reversible multielectron transfer I^-/IO_3^- cathode enabled by a hetero-halogen electrolyte for high-energy-density aqueous batteries. *Nat. Energy* **2024**, *9*, 714−724.

(12) Li, X.; Xu, W.; Zhi, C. Halogen-powered static conversion chemistry. *Nat. Rev. Chem* **2024**, *8* (5), 359−375.

(13) Dong, D.; Wang, T.; Sun, Y.; Fan, J.; Lu, Y.-C. Hydrotropic solubilization of zinc acetates for sustainable aqueous battery electrolytes. *Nat. Sustain.* **2023**, *6* (11), 1474−1484.

(14) Li, Z.; Lu, Y.-C. Polysulfide-based redox flow batteries with long life and low levelized cost enabled by charge-reinforced ion-selective membranes. *Nat. Energy* **2021**, *6* (5), 517−528.

(15) Shen, Z.; Jin, X.; Tian, J.; Li, M.; Yuan, Y.; Zhang, S.; Fang, S.; Fan, X.; Xu, W.; Lu, H.; et al. Cation-doped ZnS catalysts for polysulfide conversion in lithium−sulfur batteries. *Nat. Catal.* **2022**, *5* (6), 555−563.

(16) Zhou, J.; Chandrappa, M. L. H.; Tan, S.; Wang, S.; Wu, C.; Nguyen, H.; Wang, C.; Liu, H.; Yu, S.; Miller, Q. R. S.; et al. Healable and conductive sulfur iodide for solid-state Li−S batteries. *Nature* **2024**, *627* (8003), 301−305.

(17) Li, H.; Meng, R.; Ye, C.; Tadich, A.; Hua, W.; Gu, Q.; Johannessen, B.; Chen, X.; Davey, K.; Qiao, S.-Z. Developing high-power Li||S batteries via transition metal/carbon nanocomposite electrocatalyst engineering. *Nat. Nanotechnol.* **2024**, *19*, 792−799.

(18) Zhang, T.; Zhang, L.; Hou, Y. MXenes: Synthesis strategies and lithium-sulfur battery applications. *eScience* **2022**, *2* (2), 164−182.

(19) Li, X.-Y.; Feng, S.; Zhao, C.-X.; Cheng, Q.; Chen, Z.-X.; Sun, S.-Y.; Chen, X.; Zhang, X.-Q.; Li, B.-Q.; Huang, J.-Q.; et al. Regulating lithium salt to inhibit surface gelation on an electrocatalyst for high-energy-density lithium−sulfur batteries. *J. Am. Chem. Soc.* **2022**, *144* (32), 14638−14646.

(20) Hua, W.; Shang, T.; Li, H.; Sun, Y.; Guo, Y.; Xia, J.; Geng, C.; Hu, Z.; Peng, L.; Han, Z.; et al. Optimizing the p charge of S in p-block metal sulfides for sulfur reduction electrocatalysis. *Nat. Catal.* **2023**, *6* (2), 174−184.

(21) Song, Y.-W.; Shen, L.; Yao, N.; Li, X.-Y.; Bi, C.-X.; Li, Z.; Zhou, M.-Y.; Zhang, X.-Q.; Chen, X.; Li, B.-Q.; et al. Cationic lithium polysulfides in lithium−sulfur batteries. *Chem.* **2022**, *8* (11), 3031−3050.

(22) Cheng, Q.; Chen, Z.-X.; Li, X.-Y.; Hou, L.-P.; Bi, C.-X.; Zhang, X.-Q.; Huang, J.-Q.; Li, B.-Q. Constructing a 700 Wh kg^{-1}-level rechargeable lithium−sulfur pouch cell. *J. Energy Chem.* **2023**, *76*, 181−186.

(23) Zhao, M.; Li, X.-Y.; Chen, X.; Li, B.-Q.; Kaskel, S.; Zhang, Q.; Huang, J.-Q. Promoting the sulfur redox kinetics by mixed organodiselenides in high-energy-density lithium−sulfur batteries. *eScience* **2021**, *1* (1), 44−52.

(24) Liu, Y.; Elias, Y.; Meng, J.; Aurbach, D.; Zou, R.; Xia, D.; Pang, Q. Electrolyte solutions design for lithium−sulfur batteries. *Joule* **2021**, *5* (9), 2323−2364.

(25) Li, X.-Y.; Feng, S.; Zhao, M.; Zhao, C.-X.; Chen, X.; Li, B.-Q.; Huang, J.-Q.; Zhang, Q. Surface gelation on disulfide electrocatalysts in lithium−sulfur batteries. *Angew. Chem., Int. Ed.* **2022**, *61* (7), No. e202114671.

(26) Li, Z.; Li, Y.; Bi, C.-X.; Zhang, Q.-K.; Hou, L.-P.; Li, X.-Y.; Ma, J.; Zhang, X.-Q.; Li, B.-Q.; Wen, R.; et al. Construction of organic-rich

solid electrolyte interphase for long-cycling lithium−sulfur batteries. *Adv. Funct. Mater.* **2023**, *34*, 2304541.
(27) Cheng, Q.; Chen, Z.-X.; Li, X.-Y.; Bi, C.-X.; Sun, F.; Zhang, X.-Q.; Ma, X.; Li, B.-Q.; Huang, J.-Q. Deciphering the degradation mechanism of high-rate and high-energy-density lithium−sulfur pouch cells. *Adv. Energy Mater.* **2023**, *13* (42), 2301770.
(28) Peng, L.; Wei, Z.; Wan, C.; Li, J.; Chen, Z.; Zhu, D.; Baumann, D.; Liu, H.; Allen, C. S.; Xu, X.; et al. A fundamental look at electrocatalytic sulfur reduction reaction. *Nat. Catal.* **2020**, *3* (9), 762−770.
(29) Zhao, C.-X.; Li, X.-Y.; Zhao, M.; Chen, Z.-X.; Song, Y.-W.; Chen, W.-J.; Liu, J.-N.; Wang, B.; Zhang, X.-Q.; Chen, C.-M.; et al. Semi-immobilized molecular electrocatalysts for high-performance lithium−sulfur batteries. *J. Am. Chem. Soc.* **2021**, *143* (47), 19865−19872.
(30) Song, Y.-W.; Shen, L.; Li, X.-Y.; Zhao, C.-X.; Zhou, J.; Li, B.-Q.; Huang, J.-Q.; Zhang, Q. Phase equilibrium thermodynamics of lithium−sulfur batteries. *Nat. Chem. Eng.* **2024**, *1*, 588−596.
(31) Li, X.-Y.; Zhao, M.; Song, Y.-W.; Bi, C.-X.; Li, Z.; Chen, Z.-X.; Zhang, X.-Q.; Li, B.-Q.; Huang, J.-Q. Polysulfide chemistry in metal−sulfur batteries. *Chem. Soc. Rev.* **2025**, DOI: 10.1039/D4CS00318G.
(32) Su, C.-C.; He, M.; Amine, R.; Amine, K. A selection rule for hydrofluoroether electrolyte cosolvent: establishing a linear free-energy relationship in lithium−sulfur batteries. *Angew. Chem., Int. Ed.* **2019**, *58* (31), 10591−10595.
(33) Cha, E.; Patel, M. D.; Park, J.; Hwang, J.; Prasad, V.; Cho, K.; Choi, W. 2D MoS_2 as an efficient protective layer for lithium metal anodes in high-performance Li−S batteries. *Nat. Nanotechnol.* **2018**, *13* (4), 337−344.
(34) Chen, Z.-X.; Hou, L.-P.; Bi, C.-X.; Cheng, Q.; Zhang, X.-Q.; Li, B.-Q.; Huang, J.-Q. Failure analysis of high-energy-density lithium−sulfur pouch cells. *Energy Storage Mater.* **2022**, *53*, 315−321.
(35) Zhao, M.; Li, B.-Q.; Peng, H.-J.; Yuan, H.; Wei, J.-Y.; Huang, J.-Q. Lithium−sulfur batteries under lean electrolyte conditions: challenges and opportunities. *Angew. Chem., Int. Ed.* **2020**, *59* (31), 12636−12652.
(36) Hou, L.-P.; Li, Z.; Yao, N.; Bi, C.-X.; Li, B.-Q.; Chen, X.; Zhang, X.-Q.; Zhang, Q. Weakening the solvating power of solvents to encapsulate lithium polysulfides enables long-cycling lithium−sulfur batteries. *Adv. Mater.* **2022**, *34*, 2205284.
(37) Zhang, X.-Q.; Jin, Q.; Nan, Y.-L.; Hou, L.-P.; Li, B.-Q.; Chen, X.; Jin, Z.-H.; Zhang, X.-T.; Huang, J.-Q.; Zhang, Q. Electrolyte structure of lithium polysulfides with anti-reductive solvent shells for practical lithium−sulfur batteries. *Angew. Chem., Int. Ed.* **2021**, *60* (28), 15503−15509.
(38) See, K. A.; Wu, H.-L.; Lau, K. C.; Shin, M.; Cheng, L.; Balasubramanian, M.; Gallagher, K. G.; Curtiss, L. A.; Gewirth, A. A. Effect of hydrofluoroether cosolvent addition on Li solvation in acetonitrile-based solvate electrolytes and its influence on S reduction in a Li−S battery. *ACS Appl. Mater. Interfaces* **2016**, *8* (50), 34360−34371.
(39) Liu, Y.; Xu, L.; Yu, Y.; He, M.; Zhang, H.; Tang, Y.; Xiong, F.; Gao, S.; Li, A.; Wang, J.; et al. Stabilized Li−S batteries with anti-solvent-tamed quasi-solid-state reaction. *Joule* **2023**, *7* (9), 2074−2091.
(40) Su, C.-C.; He, M.; Amine, R.; Chen, Z.; Amine, K. The relationship between the relative solvating power of electrolytes and shuttling effect of lithium polysulfides in lithium−sulfur batteries. *Angew. Chem., Int. Ed.* **2018**, *57* (37), 12033−12036.
(41) Cheng, L.; Curtiss, L. A.; Zavadil, K. R.; Gewirth, A. A.; Shao, Y.; Gallagher, K. G. Sparingly solvating electrolytes for high energy density lithium−sulfur batteries. *ACS Energy Lett.* **2016**, *1* (3), 503−509.
(42) Liu, T.; Li, H.; Yue, J.; Feng, J.; Mao, M.; Zhu, X.; Hu, Y.-S.; Li, H.; Huang, X.; Chen, L.; et al. Ultralight electrolyte for high-energy lithium−sulfur pouch cells. *Angew. Chem., Int. Ed.* **2021**, *60* (32), 17547−17555.
(43) Lee, C.-W.; Pang, Q.; Ha, S.; Cheng, L.; Han, S.-D.; Zavadil, K. R.; Gallagher, K. G.; Nazar, L. F.; Balasubramanian, M. Directing the lithium−sulfur reaction pathway via sparingly solvating electrolytes for high energy density batteries. *ACS Cent. Sci.* **2017**, *3* (6), 605−613.
(44) Li, X.-Y.; Feng, S.; Song, Y.-W.; Zhao, C.-X.; Li, Z.; Chen, Z.-X.; Cheng, Q.; Chen, X.; Zhang, X.-Q.; Li, B.-Q.; et al. Kinetic evaluation on lithium polysulfide in weakly solvating electrolyte toward practical lithium−sulfur batteries. *J. Am. Chem. Soc.* **2024**, *146* (21), 14754−14764.
(45) Sun, K.; Wu, Q.; Tong, X.; Gan, H. Electrolyte with low polysulfide solubility for Li−S batteries. *ACS Appl. Energy Mater.* **2018**, *1* (6), 2608−2618.
(46) Weller, C.; Pampel, J.; Dörfler, S.; Althues, H.; Kaskel, S. Polysulfide shuttle suppression by electrolytes with low-density for high-energy lithium−sulfur batteries. *Energy Technol.* **2019**, *7* (12), 1900625.
(47) Yanagi, M.; Ueno, K.; Ando, A.; Li, S.; Matsumae, Y.; Liu, J.; Dokko, K.; Watanabe, M. Effects of polysulfide solubility and Li ion transport on performance of Li−S batteries using sparingly solvating electrolytes. *J. Electrochem. Soc.* **2020**, *167* (7), 070531.
(48) Hou, L.-P.; Zhang, X.-Q.; Yao, N.; Chen, X.; Li, B.-Q.; Shi, P.; Jin, C.-B.; Huang, J.-Q.; Zhang, Q. An encapsulating lithium-polysulfide electrolyte for practical lithium−sulfur batteries. *Chem.* **2022**, *8* (4), 1083−1098.
(49) Wang, Z.; Li, Y.; Ji, H.; Zhou, J.; Qian, T.; Yan, C. Unity of opposites between soluble and insoluble lithium polysulfides in lithium−sulfur batteries. *Adv. Mater.* **2022**, *34*, 2203699.
(50) Li, G.-X.; Koverga, V.; Nguyen, A.; Kou, R.; Ncube, M.; Jiang, H.; Wang, K.; Liao, M.; Guo, H.; Chen, J.; et al. Enhancing lithium-metal battery longevity through minimized coordinating diluent. *Nat. Energy* **2024**, *9*, 817−827.
(51) Chen, Z.-X.; Cheng, Q.; Li, X.-Y.; Li, Z.; Song, Y.-W.; Sun, F.; Zhao, M.; Zhang, X.-Q.; Li, B.-Q.; Huang, J.-Q. Cathode kinetics evaluation in lean-electrolyte lithium−sulfur batteries. *J. Am. Chem. Soc.* **2023**, *145* (30), 16449−16457.
(52) Johnson, L.; Li, C.; Liu, Z.; Chen, Y.; Freunberger, S. A.; Ashok, P. C.; Praveen, B. B.; Dholakia, K.; Tarascon, J.-M.; Bruce, P. G. The role of LiO_2 solubility in O_2 reduction in aprotic solvents and its consequences for Li−O_2 batteries. *Nat. Chem.* **2014**, *6* (12), 1091−1099.
(53) Xia, Y.; Zhou, P.; Kong, X.; Tian, J.; Zhang, W.; Yan, S.; Hou, W.-h.; Zhou, H.-Y.; Dong, H.; Chen, X.; et al. Designing an asymmetric ether-like lithium salt to enable fast-cycling high-energy lithium metal batteries. *Nat. Energy* **2023**, *8*, 934−945.
(54) Beć, K. B.; Muszyński, A. S.; Michniewicz, N.; Wrzeszcz, W.; Kotynia, A.; Hawranek, J. P. Vibrational spectra of liquid di-iso-propylether. *Vib. Spectrosc.* **2011**, *55* (1), 44−48.
(55) Shin, M.; Wu, H.-L.; Narayanan, B.; See, K. A.; Assary, R. S.; Zhu, L.; Haasch, R. T.; Zhang, S.; Zhang, Z.; Curtiss, L. A.; et al. Effect of the hydrofluoroether cosolvent structure in acetonitrile-based solvate electrolytes on the Li^+ solvation structure and Li−S battery performance. *ACS Appl. Mater. Interfaces* **2017**, *9* (45), 39357−39370.
(56) Chen, X.; Bai, Y.-K.; Zhao, C.-Z.; Shen, X.; Zhang, Q. Lithium bonds in lithium batteries. *Angew. Chem., Int. Ed.* **2020**, *59* (28), 11192−11195.
(57) Hou, T.-Z.; Xu, W.-T.; Chen, X.; Peng, H.-J.; Huang, J.-Q.; Zhang, Q. Lithium bond chemistry in lithium−sulfur batteries. *Angew. Chem., Int. Ed.* **2017**, *56* (28), 8178−8182.
(58) Liu, R.; Wei, Z.; Peng, L.; Zhang, L.; Zohar, A.; Schoeppner, R.; Wang, P.; Wan, C.; Zhu, D.; Liu, H.; et al. Establishing reaction networks in the 16-electron sulfur reduction reaction. *Nature* **2024**, *626* (7997), 98−104.
(59) Chen, J.-J.; Yuan, R.-M.; Feng, J.-M.; Zhang, Q.; Huang, J.-X.; Fu, G.; Zheng, M.-S.; Ren, B.; Dong, Q.-F. Conductive Lewis base matrix to recover the missing link of Li_2S_8 during the sulfur redox cycle in Li−S battery. *Chem. Mater.* **2015**, *27* (6), 2048−2055.
(60) Yao, N.; Chen, X.; Sun, S.-Y.; Gao, Y.-C.; Yu, L.; Gao, Y.-B.; Li, W.-L.; Zhang, Q. Identifying the lithium bond and lithium ionic bond in electrolytes. *Chem.* **2025**, *11* (1), 102254.

(61) Song, Y.-W.; Peng, Y.-Q.; Zhao, M.; Lu, Y.; Liu, J.-N.; Li, B.-Q.; Zhang, Q. Understanding the impedance response of lithium polysulfide symmetric cells. *Small Sci.* **2021**, *1* (11), 2100042.
(62) Feng, S.; Fu, Z.-H.; Chen, X.; Li, B.-Q.; Peng, H.-J.; Yao, N.; Shen, X.; Yu, L.; Gao, Y.-C.; Zhang, R.; et al. An electrocatalytic model of the sulfur reduction reaction in lithium−sulfur batteries. *Angew. Chem., Int. Ed.* **2022**, *61* (52), No. e202211448.
(63) Yao, Y.; Wang, H.; Yang, H.; Zeng, S.; Xu, R.; Liu, F.; Shi, P.; Feng, Y.; Wang, K.; Yang, W.; et al. A dual-functional conductive framework embedded with TiN-VN heterostructures for highly efficient polysulfide and lithium regulation toward stable Li−S full batteries. *Adv. Mater.* **2020**, *32* (6), 1905658.
(64) Cui, Z.; Zu, C.; Zhou, W.; Manthiram, A.; Goodenough, J. B. Mesoporous titanium nitride-enabled highly stable lithium−sulfur batteries. *Adv. Mater.* **2016**, *28* (32), 6926−6931.
(65) Zhou, T.; Lv, W.; Li, J.; Zhou, G.; Zhao, Y.; Fan, S.; Liu, B.; Li, B.; Kang, F.; Yang, Q.-H. Twinborn TiO_2−TiN heterostructures enabling smooth trapping−diffusion−conversion of polysulfides towards ultralong life lithium−sulfur batteries. *Energy Environ. Sci.* **2017**, *10* (7), 1694−1703.

https://doi.org/10.1021/jacs.5c01588
J. Am. Chem. Soc. 2025, 147, 15435−15447